chemosensors

MDPI

Article

MOF(CuBDC)-Microcantilever IR Spectroscopy for Methane Sensing with High Sensitivity and Selectivity

Seungwan Seo [1,†], Seok Bin Kwon [2,†] and Yangkyu Park [3,4,*]

[1] Medical Device Development Center, OSONG Medical Innovation Foundation, Cheongju-si 28160, Chungcheongbuk-do, Republic of Korea; seungwan@kbiohealth.kr
[2] Inorganic Light-Emitting Display Research Center, Korea Photonics Technology Institute (KOPTI), Gwangju 61007, Gyeonggi, Republic of Korea; sbkwon92@kopti.re.kr
[3] Department of Mechatronics Engineering, Chonnam National University, 50 Daehak-ro, Yeosu 59626, Jeonnam, Republic of Korea
[4] Corporate Growth Support Center, Jeonnam Yeosu Industry-University Convergence Agency, 17 Samdong 3-gil, Yeosu 59631, Jeonnam, Republic of Korea
* Correspondence: yangkyu.park@jnu.ac.kr; Tel.: +82-61-659-7713
† These authors contributed equally to this work.

Abstract: Methane, a greenhouse gas with 21 times the global warming potential of carbon dioxide, is increasingly subject to stringent emission regulations, driving the demand for high-performance methane sensors. This study proposes a novel IR spectroscopy technique based on a CuBDC-integrated microcantilever (CuBDC-microcantilever IR spectroscopy) for CH_4 sensing, offering exceptional sensitivity and selectivity. The metal-organic framework (MOF) CuBDC was synthesized on the microcantilever using a drop-and-dry method facilitated by an intense pulsed light technique. Characterization via scanning electron microscopy, X-ray diffraction, and Fourier transform infrared spectroscopy confirmed the successful formation of CuBDC on the microcantilever. The CuBDC-microcantilever IR spectroscopy demonstrated a significantly enhanced sensitivity, with a differential amplitude at the CH_4 characteristic peak approximately 13 times higher than that of a conventional Si microcantilever. Moreover, the limit of detection was determined to be as low as 14.05 ppm. The clear separation of the CH_4 characteristic peak from the water and acetone vapor peaks also emphasized the sensor's high selectivity. These findings highlight the superior sensitivity and selectivity of the proposed sensor, positioning it as a promising platform for CH_4 detection in industrial and environmental applications.

Keywords: CuBDC; microcantilever; infrared spectroscopy; methane

check for updates

Received: 25 November 2024
Revised: 31 December 2024
Accepted: 2 January 2025
Published: 3 January 2025

Citation: Seo, S.; Kwon, S.B.; Park, Y. MOF(CuBDC)-Microcantilever IR Spectroscopy for Methane Sensing with High Sensitivity and Selectivity. *Chemosensors* **2025**, *13*, 8. https://doi.org/10.3390/chemosensors13010008

Copyright: © 2025 by the authors. Licensee MDPI, Basel, Switzerland. This article is an open access article distributed under the terms and conditions of the Creative Commons Attribution (CC BY) license (https://creativecommons.org/licenses/by/4.0/).

1. Introduction

Methane, with 21 times the global warming potential of carbon dioxide, significantly contributes to extreme weather events such as heatwaves, droughts, hurricanes, and rising sea levels [1]. The stringent regulation of methane emissions worldwide [2,3] has driven increased attention to high-performance methane-sensing technologies [4,5], leading to the development of low-power, compact, and highly sensitive methane sensors [6–8]. However, like many harmful substances, methane is often present in complex mixtures containing various compounds or dissolved in water with similar molecular structures, making selective detection a significant challenge. To address this, functional groups that selectively bind to detection factors are typically employed to enhance sensor selectivity [9]. Unfortunately, reversible functional groups that react selectively with detection factors at room temperature are often unavailable, further complicating the achievement of high selectivity.

This scarcity underscores the pressing need for methane sensors that are not only highly sensitive but also highly selective, enabling effective monitoring of methane emissions.

Microcantilever infrared (IR) spectroscopy is a highly sensitive and selective chemical-sensing technology capable of detecting hazardous materials. Microcantilevers typically exhibit exceptional sensitivity in the picojoule range, with some extending to femtojoules [10], outperforming quartz crystal microbalance (QCM) and surface acoustic wave sensors, particularly in detecting low-mass quantities [11]. The low thermal mass and small dimension of the microcantilever make it highly sensitive such that minimum detectable energy up to 150 fJ was attained [12]. This technology achieves IR spectral analysis by irradiating molecules adsorbed on the microcantilever surface with an IR laser. When the vibrational modes of the adsorbed molecules resonate with the incident IR laser, the molecules emit thermal energy, inducing deformation in the highly temperature-sensitive microcantilever. This deformation varies with the laser wavelength, producing distinct spectra for different molecules and significantly enhancing selectivity [13]. Furthermore, wafer-level production in array formats can lower production costs and facilitate the simultaneous detection of multiple target molecules. Despite these numerous advantages, the flat surface of the microcantilever could present limitations for the adsorption of target substances.

Metal-organic frameworks (MOFs) are crystalline porous materials with structural networks that coordinate metal ions with organic ligands. Their well-dispersed metal ions, highly ordered internal architecture, and pore sizes comparable to biomolecules impart remarkable physicochemical properties [14]. These features have enabled diverse applications in catalysis, drug delivery, and sensing, and as templates for nanomaterial synthesis [14,15]. Notably, the high adsorption capacity and large surface area of MOFs make them particularly effective as active sites for detecting chemical substances [8].

Recent research has sought to enhance gas-detection capabilities by leveraging the high adsorption capacity of MOFs in combination with the high sensitivity of microcantilevers [16–18]. However, these sensors have been limited by their reliance on low-dimensional data, such as resonant frequency shifts of the microcantilevers, which constrains their selectivity.

This paper presents a novel approach using a MOF, copper benzene-1,4-dicarboxylate (CuBDC), coated on a microcantilever for IR spectroscopy (CuBDC-microcantilever IR spectroscopy) to achieve highly sensitive and selective methane detection. CuBDC is synthesized efficiently on a microcantilever via an intense pulsed light (IPL) heating technique, producing a highly porous MOF capable of methane detection at room temperature and atmospheric pressure. The in situ fabrication of CuBDC on the microcantilever is demonstrated, along with detailed characterization of the synthesized material. Furthermore, the IR spectra of methane are measured using the proposed MOF-microcantilever IR spectroscopy, showcasing its superior sensitivity and selectivity. This study represents the first integration of IR spectroscopy with a MOF microcantilever. Moreover, no prior work has reported methane-sensing microcantilever-based IR sensors.

2. Materials and Methods

2.1. Materials

Methane (CH_4 0.1%) as the target gas was purchased from Air Liquide (Paris, France). The following reagents were used without additional purification for the synthesis of CuBDC on a Si microcantilever array (OCTOSENSIS, Miromotive, Germany): sodium hydroxide (NaOH, 97%, VWR, Radnor, PA, USA), terephthalic acid (benzene-1,4-dicarboxylic acid, BDC, 98+%, VWR, Radnor, PA, USA), ammonium persulfate ($(NH_4)_2S_2O_8$, 98%, Sigma-Aldrich, Burlington, MA, USA), N,N-dimethylformamide (DMF, 99.8%, VWR, Radnor, PA, USA), methanol (99%, VWR, Radnor, PA, USA), acetone (99%, VWR, Radnor, PA,

USA), ethanol (98%, VWR, Radnor, PA, USA), isopropyl alcohol (IPA, VWR, Radnor, PA, USA), and distilled deionized water (DDW). The selected microcantilever had a spring constant of less than 23 mN/m, with detailed specifications provided in Table 1.

Table 1. Microcantilever specifications.

	Specifications
Cantilever thickness	1 μm
Cantilever length	500 μm
Cantilever width	90 μm
Body size	3000 × 2500 μm
Material	Si
Number of cantilevers in a chip	8

2.2. Synthesis of CuBDC on Microcantilever

Figure 1 depicts the fabrication process of the CuBDC microcantilever. The microcantilever array was sequentially cleaned with acetone, methanol, IPA, and DDW. A thin Cr/Cu layer was sputter-coated onto the top side of the microcantilever. The Cr layer was utilized to enhance adhesion between the Si and Cu. To create a strong oxidizing solution, 4 mL of NaOH (10 M), 2 mL of $(NH_4)_2S_2O_8$(1 M), and 9 mL of DDW were mixed. The Cu-coated microcantilever was immersed in this solution for 10 min to oxidize the Cu layer, forming $Cu(OH)_2$ nanowires on its surface. For the BDC precursor solution (0.16 M), 0.4 g of BDC was dissolved in 15 mL of DMF and stirred for approximately 1 h. The solution was drop-cast onto the $Cu(OH)_2$ nanowires, and the coated nanowires were exposed to multiple intense pulsed light (IPL) flashes from a xenon flashlight (Speedotron, Chicago, IL, USA) with a 6 ms duration and energy ranging from 3 to 27 J per flash, fully converting the nanowires into a CuBDC layer. The bottom side of the fabricated CuBDC microcantilever was then sputtered with Cr/Au to induce a bimetallic effect and serve as a reflective layer. Finally, the CuBDC microcantilever was cleaned and dried overnight in a vacuum oven at 70 °C to remove residual solvents from the CuBDC pores.

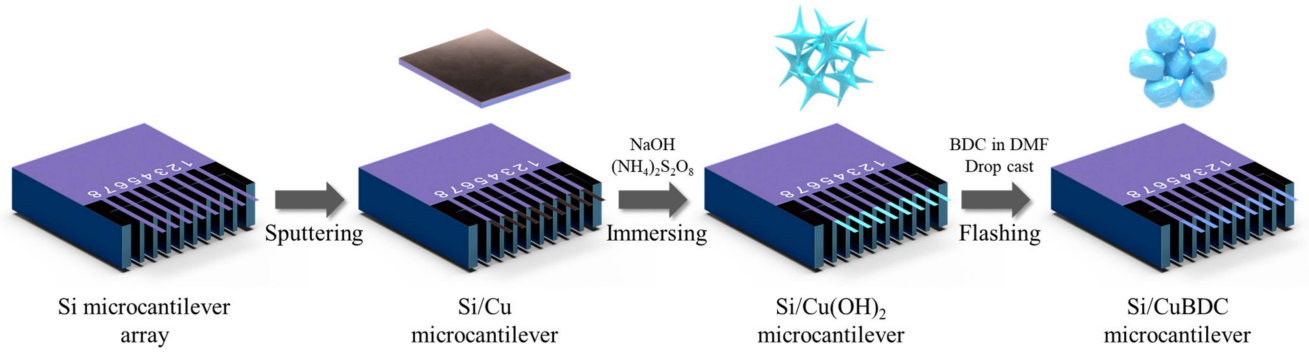


Figure 1. Fabrication process of CuBDC microcantilever.

2.3. Characterization of CuBDC on Microcantilever

The crystalline structure of the synthesized CuBDC was analyzed using X-ray diffraction (XRD, Rigaku Multiflex, CAE, Austin, TX, USA). The surface morphology was characterized using a field emission scanning electron microscope (FE-SEM, Quanta™ 250, Philips, Amsterdam, The Netherlands). Additionally, the standard Fourier transform infrared (FTIR) spectrum of the CuBDC was recorded in attenuated total reflection mode using an FTIR spectrometer (IRAffinity, SHIMADZU, Kyoto, Japan).

2.4. Experimental Setup for CH_4 Sensing

CH_4-sensing experiments were conducted at room temperature and atmospheric pressure, as shown schematically in Figure 2. Two gas cylinders were utilized: one (cylinder 1) containing a mixture of 0.1% CH_4 with N_2 as the balance gas and the other (cylinder 2) containing pure N_2 (99.999%). A bubbler filled with DDW was incorporated to evaluate the selectivity of CH_4 sensing in the presence of water or acetone vapor. To remove residual contaminants from the CuBDC, the flow cell was initially flushed with 300 cm^3/min of N_2 from cylinder 2 for 1 h. Following this, CH_4 gas from cylinder 1 was introduced into the flow cell at controlled ratios using mass flow controllers (MFC, AtoVac GMC1200, Suwon, Republic of Korea). The sensor's sensitivity was evaluated by analyzing various CH_4 concentrations under these controlled conditions.

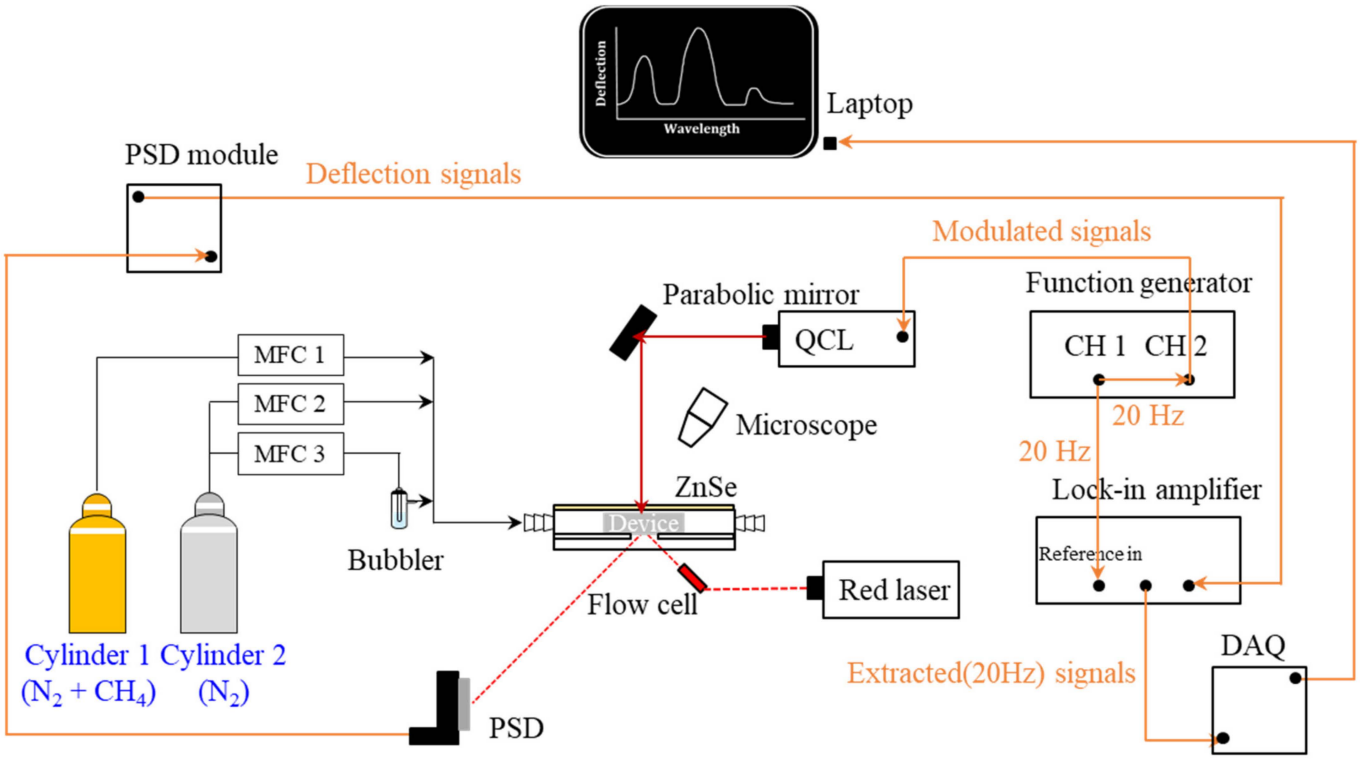


Figure 2. Experimental setup for measuring IR spectra of CH_4.

The gas concentration (G_{ppm}) can be expressed as

$$G_{ppm} = \frac{M_{CH4}F_{c1}}{M_{CH4}F_{c1} + M_{N2}F_{c1} + F_{c2} + F_{Bubbler}} \times 10^6, \quad (1)$$

where M_{CH4} and M_{N2} represent the mole fractions of CH_4 and N_2 in cylinder 1, respectively. F_{c1} and F_{c2} denote the flow rates of MFC 1 and MFC 2, respectively. The total output flow rate from the bubbler ($F_{Bubbler}$) is described as [19]

$$F_{Bubbler} = F_{c3} + F_v, \quad (2)$$

where F_{c3} is the flow rate of MFC 3. The output flow rate of the vapor (F_v) can be represented by the bubbler equation [19,20]

$$F_v = \frac{P_v}{P_{HS} - P_v} \times F_{c3}, \quad (3)$$

where P_{HS} refers to the headspace pressure above the liquid in the bubbler. P_v is the vapor pressure of the liquid and determined by the Antoine's equation

$$P_v = 10^{A-\frac{B}{C+T}}, \quad (4)$$

where T is the temperature; A, B, and C are Antoine equation constants. During the measurements, the N_2 flow rates from MFC 2 and MFC 3 were maintained at constant values of 300 cm^3/min and 1 cm^3/min, respectively. Different CH_4 concentrations were achieved by adjusting the flow rate of MFC 1.

Twenty-hertz pulses were generated on channel 1 of a two-channel function generator (model 33500, Keysight, Santa Rosa, CA, USA). These pulses were used to produce 183 kHz pulses modulated at 20 Hz with a 5% duty cycle on channel 2, preventing continuous operation of the QCL to avoid overheating and potential damage, while quasi-statistically actuating the microcantilever. The modulation signals drove the quantum cascade laser (QCL; LaserTune™, Block Engineering, Marlborough, MA, USA), which emitted a pulsed IR laser. The emitted laser was reflected by a parabolic mirror and directed toward CH_4 adsorbed on the CuBDC microcantilever. The CuBDC microcantilever was sequentially exposed to an IR wavenumber range of 1100 cm^{-1} to 1700 cm^{-1}.

The deflection of the CuBDC microcantilever was measured using the optical leverage technique. A 633 nm red laser was directed onto the Cr/Au reflection layer in the CuBDC microcantilever and reflected onto a position-sensitive detector (PSD; On-Trak, Irvine, CA, USA). The deflection signals from the PSD were processed with a lock-in amplifier (SR850, Stanford Research Systems, Sunnyvale, CA, USA) to extract the 20 Hz reference frequency, filtering out all other frequency components. The extracted signals were then sent to a data acquisition board (DAQ; National Instruments, Austin, TX, USA) and collected on a laptop using a custom LabVIEW program (LabVIEW 2024).

3. Results and Discussion

3.1. In Situ Fabrication and Characteristics of CuBDC Microcantilever

Various methods are employed to fabricate MOFs, including spray coating [15], layer-by-layer assembly [21], electrochemical deposition [22], solvothermal growth [23], and gel–vapor deposition [24]. These techniques offer advantages such as high porosity, tunable pore sizes, and tailored physical and chemical properties. However, the preparation of MOF layers often involves extended processing times, and the bonding strength between the MOF layer and the substrate may be insufficient.

In this study, Cu-based MOFs were synthesized directly onto Si microcantilever arrays using the IPL technique, streamlining the fabrication process and improving the adhesion strength between the MOF layer and the microcantilever. A thin layer of Cu was sputter-coated onto the microcantilever. An oxidizing aqueous solution was then dispensed onto the sputtered Cu layer, leading to the oxidation of Cu and the formation of $Cu(OH)_2$ nanowires. This oxidation step is critical, as the conversion from metal-to-metal hydroxide significantly increases the surface area compared to that of the flat metal microcantilever. The enhanced surface area provides a greater number of active sites for chemical reactions, facilitating the coordination of metal ions with organic ligands and promoting the formation of MOFs. Figure 3 illustrates the conversion process of Cu to $Cu(OH)_2$ over time. Initially, minimal surface changes were observed; however, as the conversion time approached 30 min, the formation of $Cu(OH)_2$ nanowires became apparent. The increase in surface area is clearly visible in Figure 3c. Furthermore, as reported previously [25], the binding energy of Cu ions in metallic Cu was measured at 932.61 eV, whereas in $Cu(OH)_2$ it was 916.5 eV. The reduced energy indicates that the fabricated $Cu(OH)_2$ nanowires offer improved interaction and provide an optimized surface for efficient MOF synthesis.

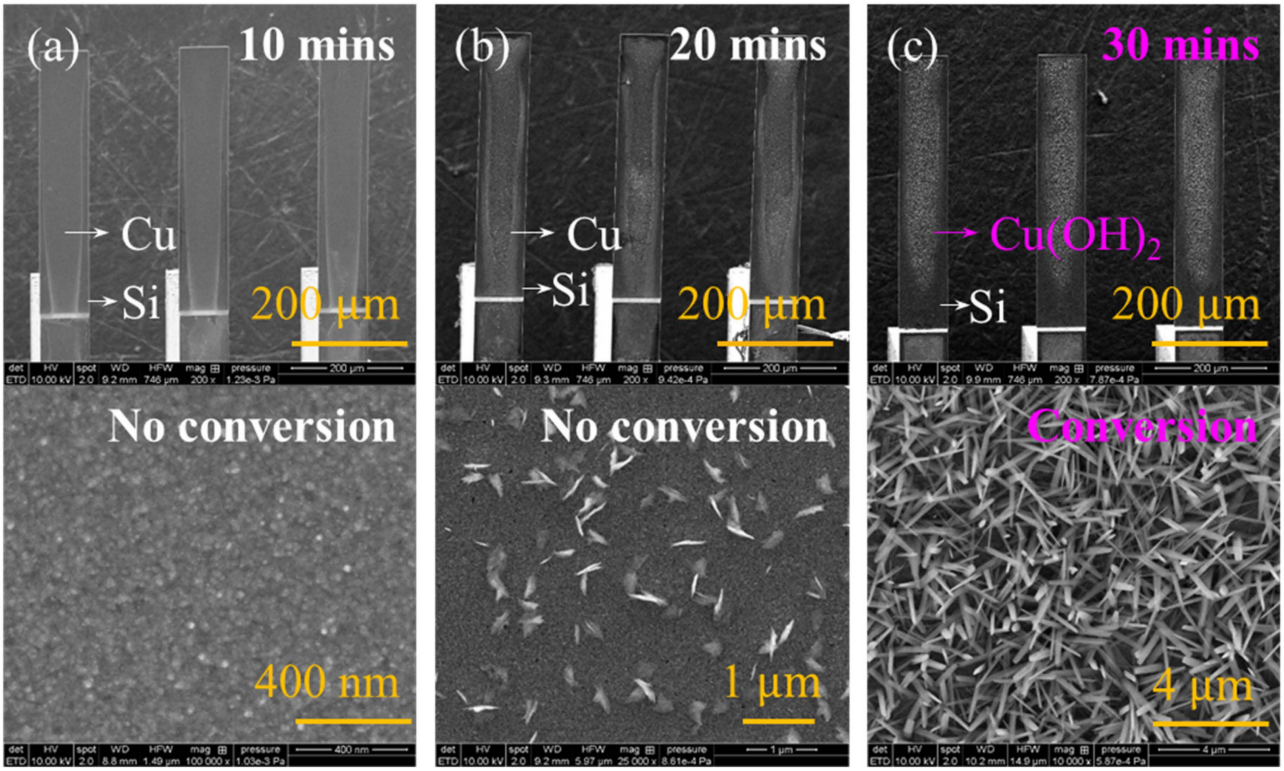


Figure 3. SEM images illustrating the conversion process from Cu to $Cu(OH)_2$ over time: (**a**) 10 min, (**b**) 20 min, and (**c**) 30 min. $Cu(OH)_2$ nanowires with a larger surface area were formed after a 30 min conversion. The first and second rows show images taken at lower and higher magnifications, respectively. Only three of the eight microcantilevers are displayed. The images were taken from a top-view perspective. However, during the fixation of the microcantilever to the chip holder, it was not perfectly horizontal, which may give the appearance of an inclination angle.

After the formation of the $Cu(OH)_2$ nanowires on the microcantilever, a BDC precursor solution was dispensed onto the nanowires, followed by irradiation with multiple IPL flashes. While the microcantilever's low spring constant allows for high sensitivity, it also makes the structure fragile, necessitating the careful adjustment of IPL power settings. At energy levels exceeding 10 J, cantilever breakage was observed due to the high pulse energy applied over a short duration. To mitigate this risk, the minimum energy setting of 3 J was employed, with repeated applications, to achieve the desired results without damaging the cantilever. Figure 4 illustrates the formation of MOF crystals as the number of IPL repetitions increased. CuBDC crystals were well developed after 160 repetitions, as shown in Figure 4d. Since each flash lasted approximately one second, the entire synthesis process for the IPL was completed in under three minutes.

Structural transformations were confirmed using XRD, as shown in Figure 5. The XRD signals of $Cu(OH)_2$ and CuBDC were measured after 30 min of oxidation (Figure 3c) and 160 IPL repetitions (Figure 4d), respectively. After oxidation, a distinct peak at $2\theta = 17.04°$, corresponding to the (202) plane of $Cu(OH)_2$ nanowires, indicated the successful oxidation of the sputtered copper layer. This structural change highlights the increased surface area and reactivity essential for MOF synthesis. Following several IPL flashes, additional peaks appeared at $2\theta = 7.7°$ and 17.68° [26], associated with the (001) and (002) planes of CuBDC, respectively [27,28]. The XRD peaks observed at approximately 16° and 24° in Figure 4 are consistent with the previously reported diffraction patterns of CuBDC crystallites formed via heteroepitaxial growth on $Cu(OH)_2$ substrates. This result highlights the role of lattice matching in facilitating the oriented crystallization of the MOF structure [29]. These

diffractions confirm the formation of a well-ordered crystalline structure, demonstrating the effectiveness of the IPL method for MOF crystallization. Furthermore, the pronounced peaks signify the robustness of the CuBDC framework, making it suitable for applications that demand precise structural characteristics.

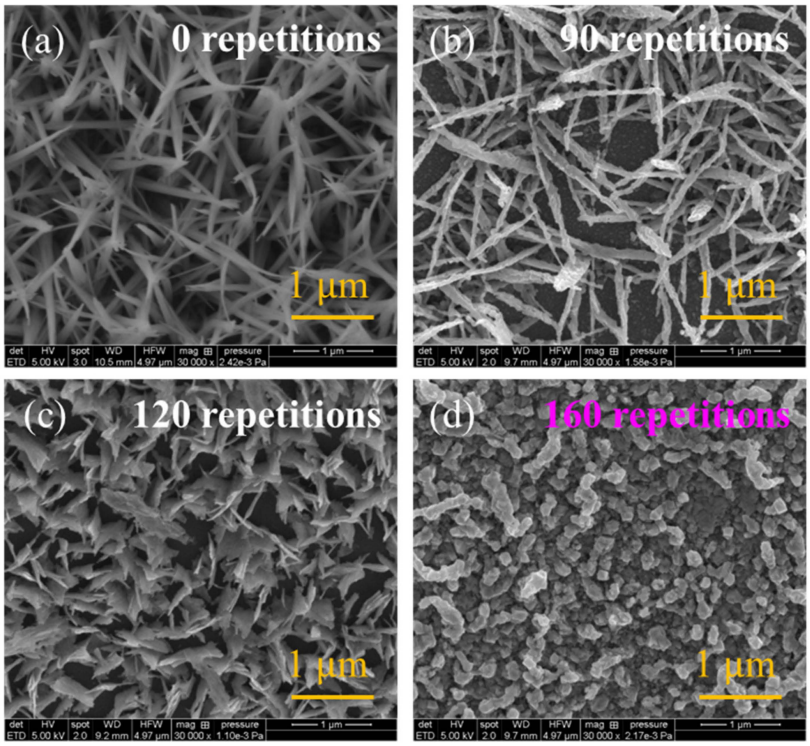


Figure 4. SEM images depicting the conversion process from $Cu(OH)_2$ to CuBDC as a function of flash repetition: (**a**) 0 repetitions, (**b**) 90 repetitions, (**c**) 120 repetitions, and (**d**) 160 repetitions. CuBDC crystals were formed after 160 repetitions.

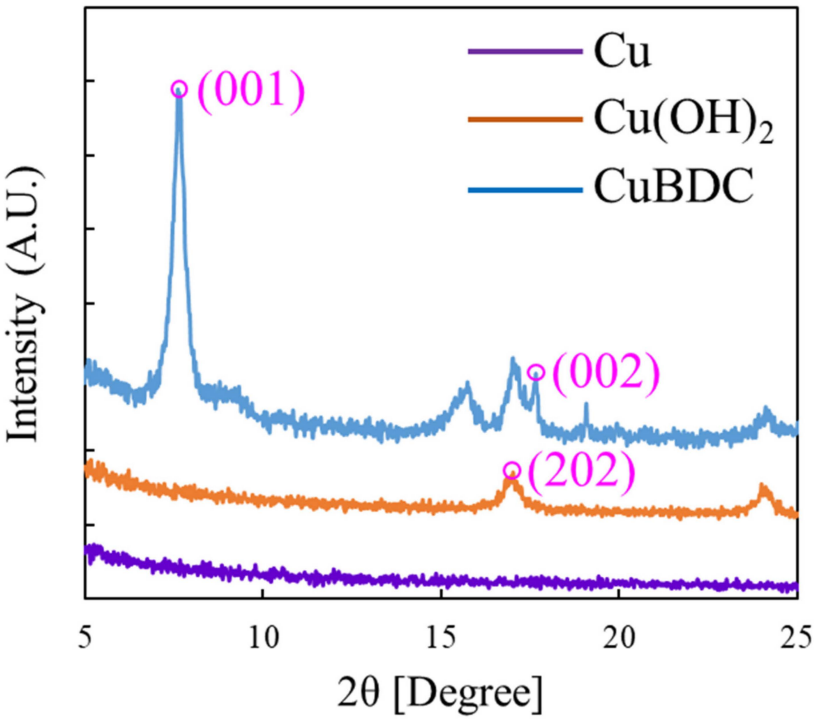


Figure 5. The XRD patterns comparing the fabricated CuBDC, $Cu(OH)_2$, and Cu.

The XRD analysis of the synthesized Cu-BDC layer indicates a monoclinic structure (space group C2/m) with lattice constants of a = 11.41 Å, b = 14.27 Å, c = 7.78 Å, $\alpha = 90°$, $\beta = 108.12°$, $\gamma = 90°$, consistent with the previous studies [30,31]. The crystallite size, calculated using the Scherrer equation at the (001) peak ($2\theta = 7.7°$) with a full width at half maximum (FWHM) of 0.78°, was determined to be approximately 10.2 nm, highlighting the nanoscale dimensions of the Cu-BDC crystallites. Figure 6 presents a visualization of the CuBDC structure based on the CCDC-687690 crystallographic data.

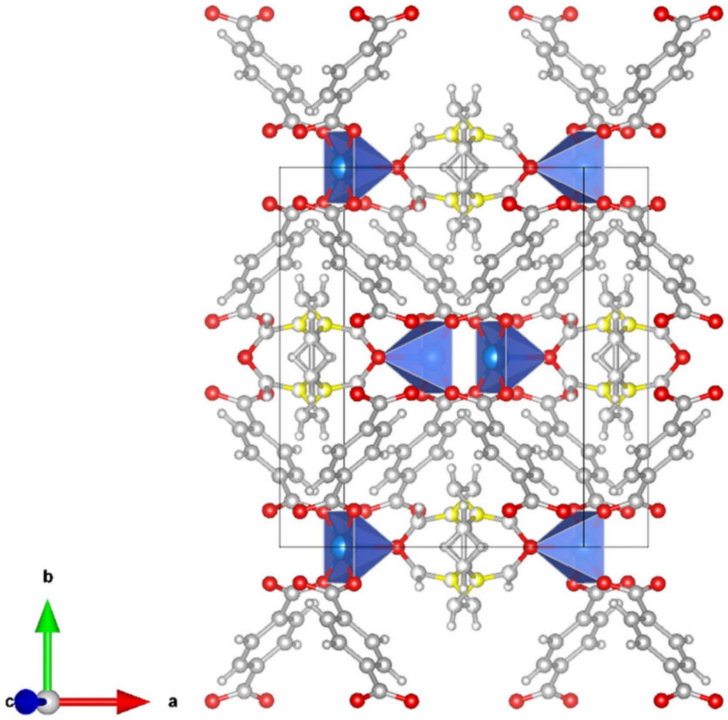


Figure 6. The crystal structure of the CuBDC (CCDC-687690).

The XRD patterns of the final CuBDC structure suggest a near-complete conversion. However, the possibility of minor residual $Cu(OH)_2$ or intermediate phases cannot be completely excluded. Future studies will employ X-ray photoelectron spectroscopy to quantitatively assess the degree of oxidation and to confirm the presence of any residual or intermediate phases, providing a more comprehensive understanding of the transformation process.

The FTIR spectra of the CuBDC layer, shown in Figure 7, further validate the presence of CuBDC [27,28]. The peaks at 734 and 1025 cm^{-1} were attributed to the γ(C–H) and δ(C–H) vibrations of the aromatic rings, respectively, confirming the incorporation of the organic linker in the synthesized CuBDC. A band at 1505 cm^{-1} was associated with the phenyl group, while the intense peaks at 1396 and 1569 cm^{-1} corresponded to the symmetric and asymmetric stretching modes of the coordinated carboxylic acid group, respectively. These characteristic peaks closely align with those reported in previous studies [28,32], confirming the successful synthesis of the CuBDC layer. Also, a peak observed in the 550–600 cm^{-1} range in the FT-IR spectrum corresponds to Cu-O bond vibrations, confirming the coordination between the Cu center and carboxylate groups in the BDC ligand. This peak supports the successful formation of the CuBDC structure.

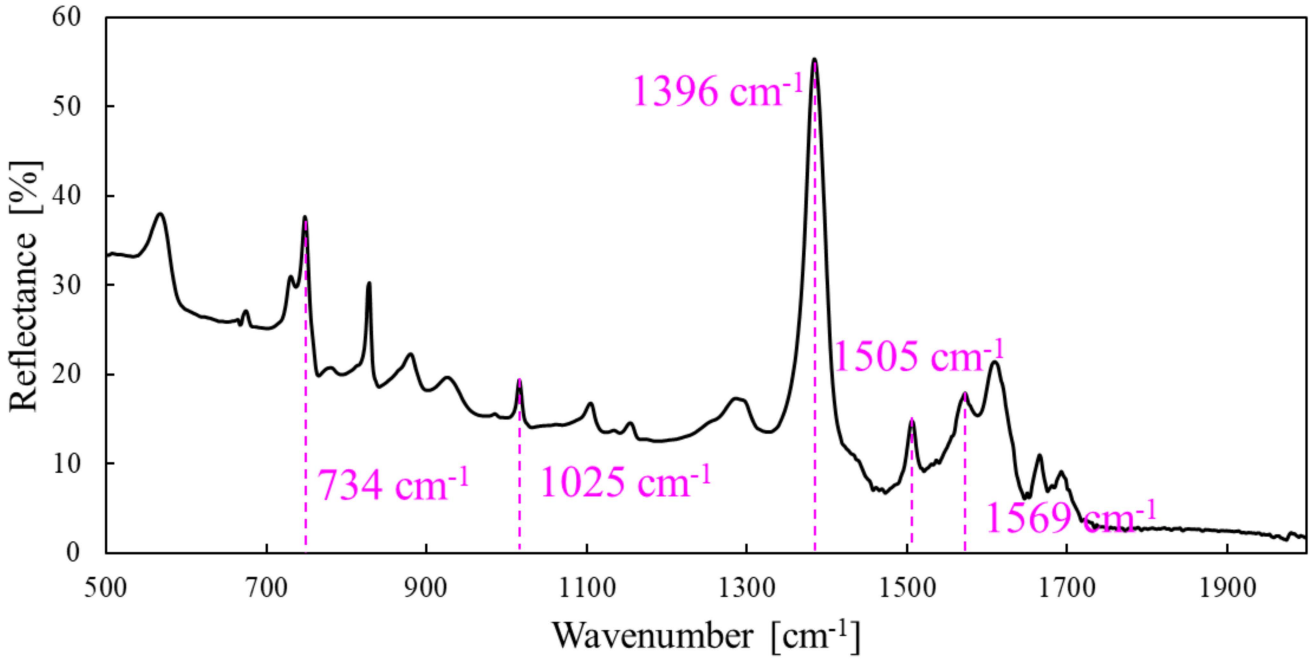


Figure 7. A FTIR analysis of the fabricated CuBDC.

The SEM, XRD, and FTIR analyses provided strong evidence for the successful synthesis of CuBDC on the microcantilever, indicating the presence of the organic ligand and key functional groups essential for the framework. These analyses also demonstrated the effectiveness of the IPL technique for the integration of the CuBDC structure into the microcantilever. Figure 8 presents an overall view of the fabricated CuBDC microcantilever. The microcantilever positioned at the far right was used to measure the IR spectrum of CH_4.

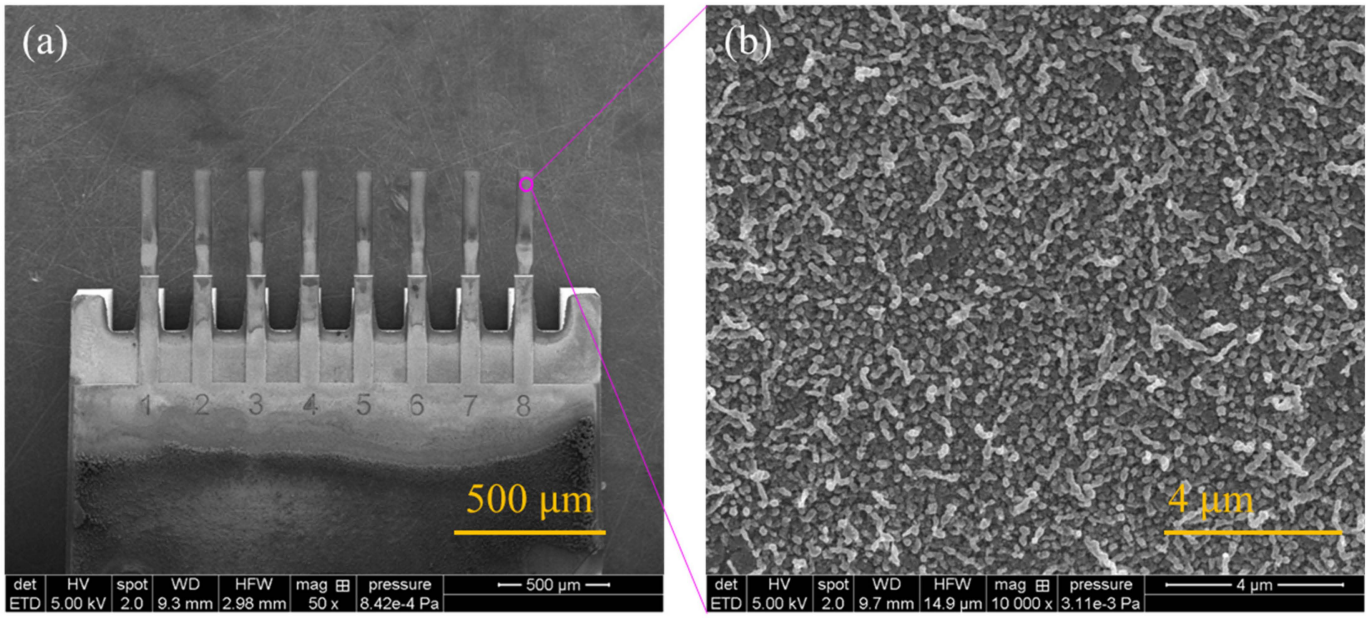


Figure 8. SEM images of the fabricated CuBDC microcantilever: (**a**) overall view and (**b**) magnified view.

3.2. CuBDC-Microcantilever IR Spectroscopy

The IR spectrum of CH_4 was measured using the proposed CuBDC-microcantilever IR spectroscopy. Initially, 300 cm^3/min of N_2 from MFC 2 was passed through the flow cell for 1 h, and the reference IR spectrum, measured with only N_2, was recorded using the experimental setup shown in Figure 2. Subsequently, 1 cm^3/min of N_2 from MFC 3

was directed into the bubbler. Next, CH_4 with N_2 as the balance gas was introduced into the flow cell. The IR spectra of CH_4 were then measured. The differential IR spectrum was obtained by subtracting the IR response of the CuBDC microcantilever exposed to target gases from the reference IR response measured with only N_2.

Figure 9 compares the IR spectra between the CuBDC microcantilever and the conventional bimetallic Si microcantilever at a CH_4 concentration of 240 ppm and water vapor at 85 ppm. While no peaks were observed in the Si microcantilever, distinct peaks were detected around 1300 cm^{-1} and 1600 cm^{-1} in the CuBDC microcantilever, corresponding to C–H bending vibrations [33,34] and O–H scissoring modes [35], respectively. In addition to the characteristic peaks, smaller irregular fluctuations are observed across the spectrum. These fluctuations might be attributed to baseline noise inherent to the experimental setup and environmental conditions. Notably, the differential amplitude of the CuBDC microcantilever at the CH_4 characteristic peak of 1300 cm^{-1} reached 42.85 mV, compared to only 3.37 mV for the Si microcantilever, resulting in an approximately 13-fold increase in sensitivity. The exceptionally high surface area and porous structure of the CuBDC MOF significantly enhanced gas adsorption, thereby improving sensitivity.

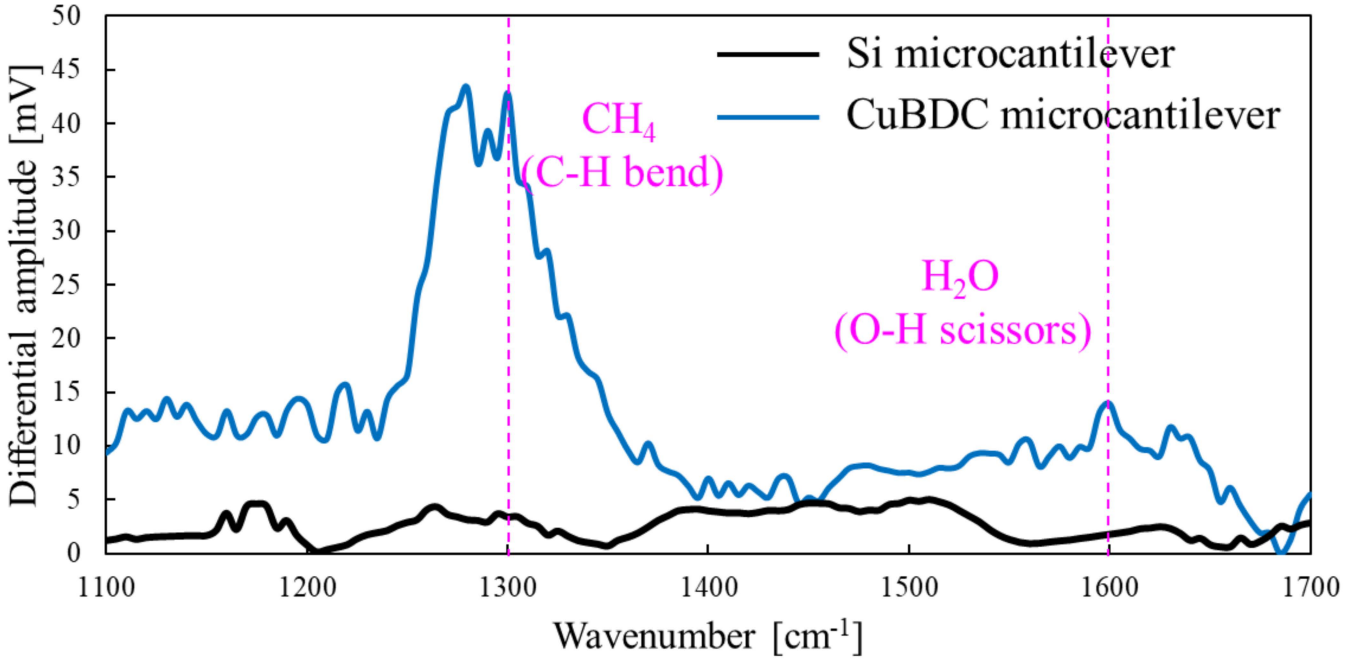


Figure 9. A comparison of the IR responses between the CuBDC and Si microcantilevers at a CH_4 concentration of 240 ppm.

Then, the bubbler was filled with acetone instead of water, and the IR spectrum was measured in a mixture of CH_4 gas (80 ppm) and acetone vapor (695 ppm). In addition to the CH_4 characteristic peak at 1300 cm^{-1}, acetone characteristic peaks were observed, as shown in Figure 10. The acetone peaks corresponded to symmetric CH_3 deformation near 1375 cm^{-1} and C–C vibrations at 1230 cm^{-1} [36]. Due to the high adsorption capacity of CuBDC for CH_4 compared to volatile organic compounds (VOCs) [8], the amplitudes for CH_4 were measured to be much stronger despite the high concentration of acetone. The clear discrimination of CH_4 from the water and acetone vapor highlights the high selectivity of the sensor.

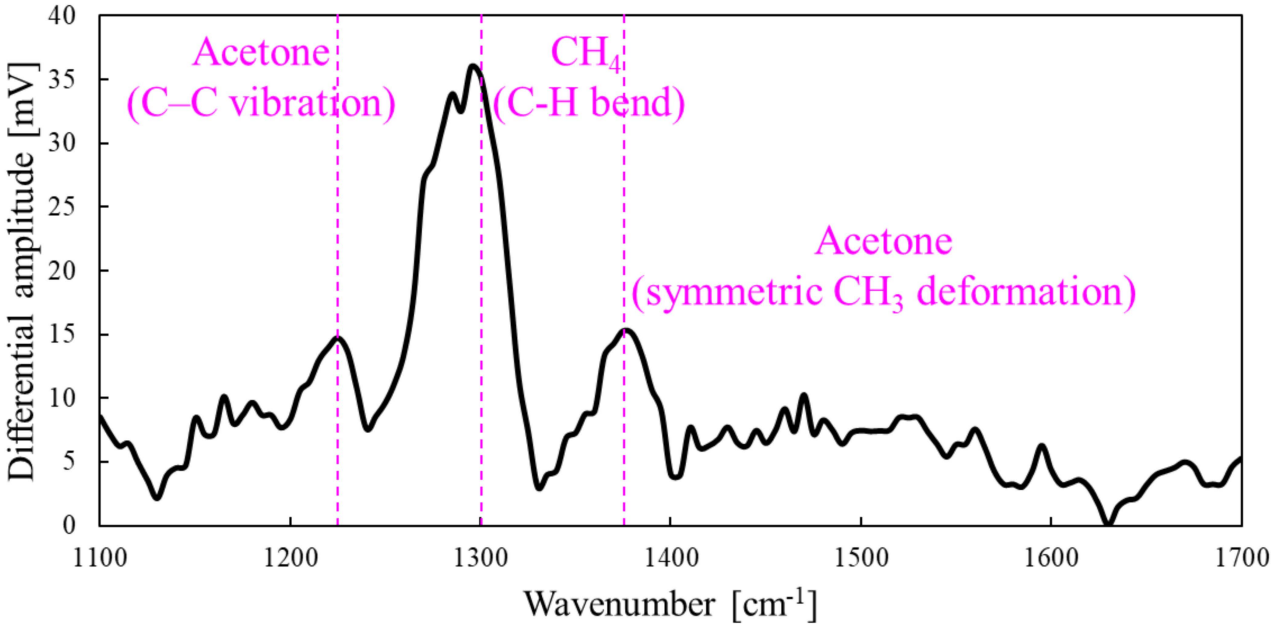


Figure 10. IR spectrum of CH_4 gas and acetone vapor mixture.

When the IR laser irradiated the adsorbed materials in the CuBDC on the bimetallic microcantilever, the molecules were resonantly excited at their corresponding IR wavelengths. This excitation elevated the temperature of the bimetallic microcantilever, which features different thermal expansion coefficients and conductivities, resulting in thermal deformation. Since molecular vibrations are highly selective, high selectivity can be achieved. The IR response was further measured for CH_4 concentrations of 80, 160, and 240 ppm. As shown in Figure 11, the CuBDC microcantilever demonstrated a clear and consistent ability to distinguish between these concentrations. While the concentration of water vapor varied from 70 ppm to 85 ppm as the CH_4 concentration changed, no significant variation was observed in the sensor's response to the water vapor. These indicate the sensor's reliable performance across a range of CH_4 levels.

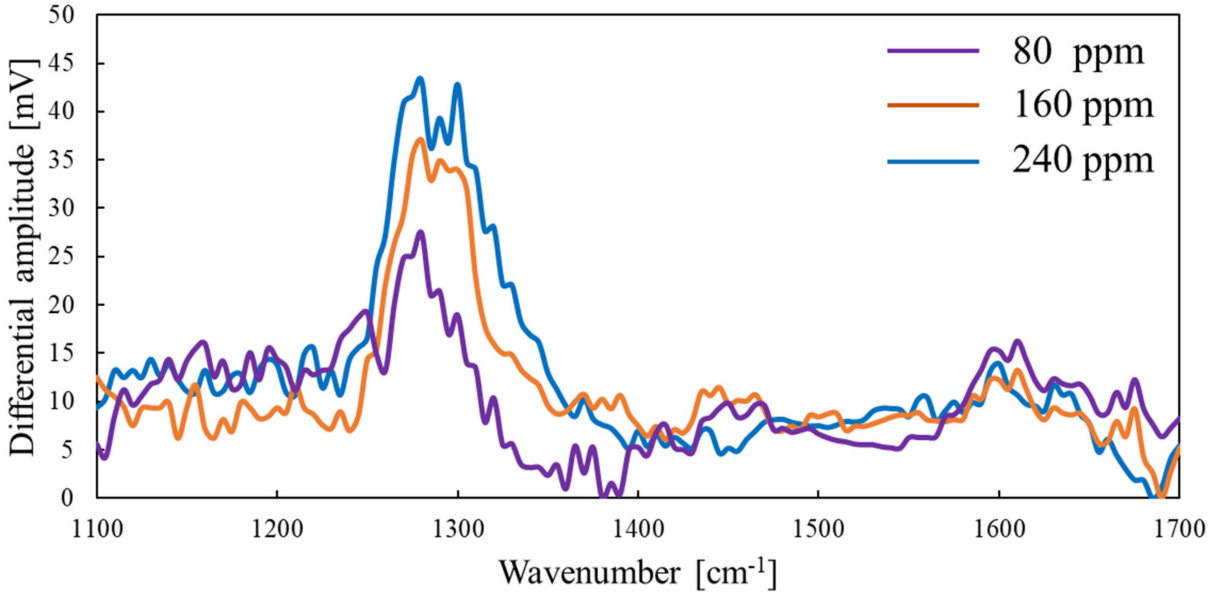


Figure 11. IR spectra of various CH_4 concentrations: 80, 160, and 240 ppm.

Figure 12 illustrates the characteristic peak amplitudes at five concentration levels. For each concentration, the peak amplitude was measured three times, and the averaged values are presented with error bars representing the standard deviation. The limit of detection (LOD) was determined by identifying the intersection of the linear fit of the peak amplitudes with the line corresponding to a signal-to-noise ratio (SNR) of 3. The LOD was estimated to be as small as 14.05 ppm. Compared to state-of-the-art CH_4 sensors that do not require a heater [37], an LOD of around 10 ppm is considered nearly the best achievable.

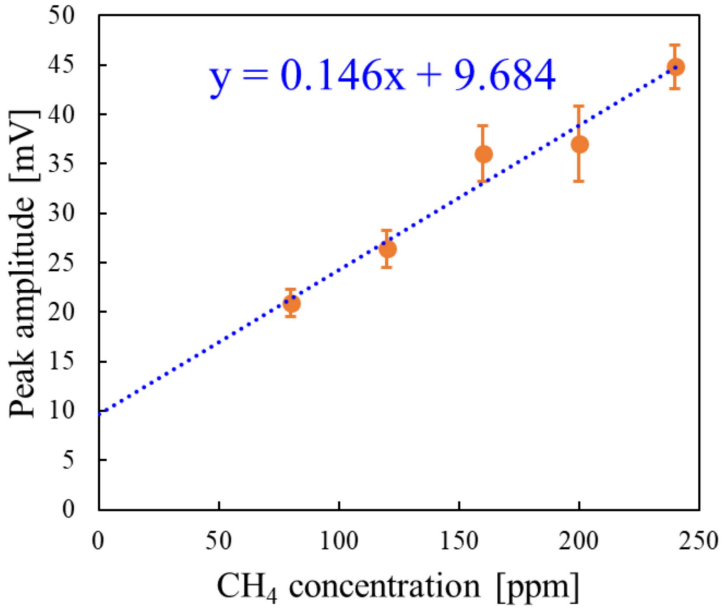


Figure 12. The peak amplitudes in the IR spectra of the CuBDC microcantilever as a function of CH_4 concentration. The error bars indicate the standard deviation derived from three measurements.

Recent developments in methane-sensing technologies include metal oxide-based sensors, which exhibit high sensitivity but require elevated operating temperatures for effective performance [38]. Carbon-based sensors, such as those utilizing functionalized carbon nanotubes or graphene, enable room-temperature operation with enhanced sensitivity through surface modifications [39]. Additionally, MOF-based sensors capitalize on their high porosity and adsorption capabilities [40]. However, selectivity remains a significant challenge for most CH_4 sensors, as designing a sensing material that is highly selective to CH_4 for practical applications is particularly difficult [37]. In contrast, our CuBDC microcantilever is less dependent on the sensing material for selectivity, as it identifies molecular vibrations.

Compared to our previous work that fabricated CuBDC on QCM [8], the minimum detectable concentration was much improved by using the microcantilever. More importantly, by combining IR spectroscopy, it became possible to distinguish various substances in mixtures, such as the target gas and other components like water or acetone.

While a previous study has combined ZIF-8 and UiO-66 with IR spectroscopy, their focus was primarily on nanoscale characterization of host–guest interactions within single MOF crystals [41]. In contrast, our study focused on a microcantilever integrated with a CuBDC MOF, specifically targeting methane detection with high sensitivity and selectivity. This approach is more aligned with real-world scenarios rather than fundamental nanoscale investigations. Consequently, our work advances MOF-based sensing technologies for industrial and environmental applications.

Instead of quasistatic microcantilever deflection induced by thermal stress, dynamic readout based on a resonance frequency shift has been widely studied for gas sensing

applications. A high sensitivity (picogram-level CH_4 detection) and high selectivity (CO detection showing 9–19 times smaller than CH_4) was demonstrated using Pt-decorated ZnO nanorods on a microcantilever [42]. Additionally, a detection limit of approximately 2 ppb for NO_2 was achieved using a piezoresistive microcantilever functionalized with self-assembled monolayer (SAM) ZnO nanorods on a silicon nanopillar array [43]. Incorporating their structures such as Pt decoration, ZnO nanorods, and SAM into our CuBDC microcantilever could further enhance its sensitivity and selectivity.

In order to enhance practicality, piezoresistive readout should be considered. Piezoresistive readout, which employs embedded piezoresistors in microcantilever arrays, provides an alternative to traditional optical readout. Unlike optical methods that require cumbersome equipment such as red lasers and PSDs, piezoresistive readout eliminates the need for such components and allows monolithic integration with integrated circuits [44].

Although the selectivity of gravimetric-based microcantilevers can be enhanced through material functionalization, observing the IR spectrum offers a more direct method for identifying molecular vibrations unique to each species. This enables a higher degree of selectivity, as IR spectroscopy provides a molecular fingerprint that allows for clear differentiation even between molecules with similar physical properties, which resonance-based methods might struggle to achieve.

Despite the promising performance of the CuBDC microcantilever sensor, several limitations must be addressed before it can be practically deployed in industrial environments such as petrochemical or oil and gas plants. Further selectivity tests under more complex and multicomponent gas conditions, including ethylene, butene, and hydrogen, are essential to evaluate the sensor's capability for selective methane detection among various gases.

Moreover, while spectroscopy offers the advantage of generating multidimensional data [45], this potential remains underutilized in the present work. By investigating various concentration ratios of mixed gases, the versatile CuBDC microcantilever sensor could capture a broader range of spectral data. Then, integrating artificial intelligence techniques with this comprehensive spectral information could enable the development of advanced analytical tools. Such tools would facilitate the precise identification of individual gas components within complex mixtures and allow for accurate quantification of their concentrations, significantly enhancing the sensor's applicability in real-world scenarios.

4. Conclusions

We introduced a IR spectroscopy method based on a CuBDC microcantilever for CH_4 sensing, demonstrating high sensitivity and selectivity. The CuBDC MOF was synthesized on a delicate microcantilever using a drop-and-dry method facilitated by an IPL technique. The crystal morphology of the synthesized CuBDC was examined through SEM imaging, its specific and ordered crystal structures were confirmed by XRD, and functional groups were identified via FTIR analysis. These characterizations collectively verified the successful formation of CuBDC on the microcantilever. The CuBDC-microcantilever IR spectroscopy exhibited a clear response to varying CH_4 concentrations and effectively distinguished CH_4 peaks from water and acetone vapor peaks. Compared to conventional Si microcantilevers, the CuBDC microcantilever demonstrated significantly higher sensitivity and selectivity for CH_4 detection, underscoring its potential for gas detection applications. In conclusion, the CuBDC microcantilever represents a promising platform for CH_4 sensing in diverse practical applications.

Author Contributions: Conceptualization: Y.P.; methodology: S.S. and S.B.K.; formal analysis: S.S.; investigation: S.S. and S.B.K.; writing—original draft preparation: Y.P. and S.S.; writing—review and editing: Y.P. and S.B.K.; visualization: S.S. and S.B.K.; supervision: Y.P.; project administration: Y.P.; funding acquisition: Y.P. All authors have read and agreed to the published version of the manuscript.

Funding: This work was supported by the Korea Planning & Evaluation Institute of Industrial Technology, funded by the Ministry of the Interior and Safety (MOIS, Republic of Korea) (No. RS-2024-00409733), and by the National Research Foundation of Korea (NRF) grant, funded by the Korean government (MSIT, Republic of Korea) (No. RS-2023-00210498). This work was also supported by a Chonnam National University (Smart Plant Reliability Center) grant funded by the Ministry of Education (MOE, Republic of Korea) (No. 2020R1A6C101B197).

Institutional Review Board Statement: Not applicable.

Informed Consent Statement: Not applicable.

Data Availability Statement: Data are contained within the article.

Acknowledgments: The authors thank the Jeonnam Yeosu Industry-University Convergence Agency for providing cleanroom facilities.

Conflicts of Interest: The authors declare no conflicts of interest. S.S. and Y.P., respectively, are employed by the non-profit organizations OSONG Medical Innovation Foundation and Jeonnam Yeosu Industry-University Convergence Agency. The funders had no role in the design of the study; in the collection, analyses, or interpretation of data; in the writing of the manuscript; or in the decision to publish the results.

References

1. Mohajan, H. Dangerous Effects of Methane Gas in Atmosphere. *Int. J. Econ. Political Integr.* **2012**, *1*, 3–10.
2. Tao, S.; Chen, S.; Pan, Z. Current status, challenges, and policy suggestions for coalbed methane industry development in China: A review. *Energy Sci. Eng.* **2019**, *7*, 1059–1074. [CrossRef]
3. Johnson, M.R.; Tyner, D.R. A case study in competing methane regulations: Will Canada's and Alberta's contrasting regulations achieve equivalent reductions. *Elem. Sci. Anth.* **2020**, *8*, 7. [CrossRef]
4. Rashid, K.; Speck, A.; Osedach, T.P.; Perroni, D.V.; Pomerantz, A.E. Optimized inspection of upstream oil and gas methane emissions using airborne LiDAR surveillance. *Appl. Energy* **2020**, *275*, 115327. [CrossRef]
5. Tuzson, B.; Graf, M.; Ravelid, J.; Scheidegger, P.; Kupferschmid, A.; Looser, H.; Morales, R.P.; Emmenegger, L. A compact QCL spectrometer for mobile, high-precision methane sensing aboard drones. *Atmos. Meas. Tech.* **2020**, *13*, 4715–4726. [CrossRef]
6. Das, I.; Bhattacharyya, R.; Saha, H.; Ghosh, S. Enhanced response of co-planar MEMS microheater-based methane gas sensor. *IEEE Sens. J.* **2020**, *20*, 14132–14140. [CrossRef]
7. Strahl, T.; Steinebrunner, J.; Weber, C.; Wöllenstein, J.; Schmitt, K. Photoacoustic methane detection inside a MEMS microphone. *Photoacoustics* **2023**, *29*, 100428. [CrossRef]
8. Park, Y.; Homayoonnia, S.; Kim, S.; Kim, H.W. In-situ fabrication of Cu-BDC on a quartz crystal microbalance for methane sensing at room temperature. *J. Incl. Phenom. Macrocycl. Chem.* **2021**, *101*, 321–327. [CrossRef]
9. Li, J.; Zhao, H.; Wang, Y.; Zhou, Y. Approaches for selectivity improvement of conductometric gas sensors: An overview. *Sens. Diagn.* **2024**, *3*, 336–353. [CrossRef]
10. Perazzo, T.; Mao, M.; Kwon, O.; Majumdar, A.; Varesi, J.; Norton, P. Infrared vision using uncooled micro-optomechanical camera. *Appl. Phys. Lett.* **1999**, *74*, 3567–3569. [CrossRef]
11. Thundat, T.; Majumdar, A. Microcantilevers for physical, chemical, and biological sensing. In *Sensors and Sensing in Biology and Engineering*; Springer: Berlin/Heidelberg, Germany, 2003; pp. 337–355.
12. Barnes, J.; Stephenson, R.; Woodburn, C.; O'shea, S.; Welland, M.; Rayment, T.; Gimzewski, J.; Gerber, C. A femtojoule calorimeter using micromechanical sensors. *Rev. Sci. Instrum.* **1994**, *65*, 3793–3798. [CrossRef]
13. Jeong, H.-J.; Park, C.-J.; Kim, K.; Park, Y. Discrimination of Explosive Residues by Standoff Sensing Using Anodic Aluminum Oxide Microcantilever Laser Absorption Spectroscopy with Kernel-Based Machine Learning. *Sensors* **2024**, *24*, 5867. [CrossRef] [PubMed]
14. Olorunyomi, J.F.; Geh, S.T.; Caruso, R.A.; Doherty, C.M. Metal–organic frameworks for chemical sensing devices. *Mater. Horiz.* **2021**, *8*, 2387–2419. [CrossRef] [PubMed]

15. Ellis, J.E.; Crawford, S.E.; Kim, K.-J. Metal–organic framework thin films as versatile chemical sensing materials. *Mater. Adv.* **2021**, *2*, 6169–6196. [CrossRef]
16. Cai, S.; Li, W.; Xu, P.; Xia, X.; Yu, H.; Zhang, S.; Li, X. In situ construction of metal–organic framework (MOF) UiO-66 film on Parylene-patterned resonant microcantilever for trace organophosphorus molecules detection. *Analyst* **2019**, *144*, 3729–3735. [CrossRef]
17. Venkatasubramanian, A.; Lee, J.-H.; Stavila, V.; Robinson, A.; Allendorf, M.D.; Hesketh, P.J. MOF@ MEMS: Design optimization for high sensitivity chemical detection. *Sens. Actuators B Chem.* **2012**, *168*, 256–262. [CrossRef]
18. Yim, C.; Lee, M.; Yun, M.; Kim, G.-H.; Kim, K.T.; Jeon, S. CO2-selective nanoporous metal-organic framework microcantilevers. *Sci. Rep.* **2015**, *5*, 10674. [CrossRef]
19. Mayer, B.; Collins, C.C.; Walton, M. Transient analysis of carrier gas saturation in liquid source vapor generators. *J. Vac. Sci. Technol. A Vac. Surf. Films* **2001**, *19*, 329–344. [CrossRef]
20. Love, A.; Middleman, S.; Hochberg, A.K. The dynamics of bubblers as vapor delivery systems. *J. Cryst. Growth* **1993**, *129*, 119–133. [CrossRef]
21. Chen, D.-H.; Gliemann, H.; Wöll, C. Layer-by-layer assembly of metal-organic framework thin films: Fabrication and advanced applications. *Chem. Phys. Rev.* **2023**, *4*, 011305. [CrossRef]
22. Ameloot, R.; Stappers, L.; Fransaer, J.; Alaerts, L.; Sels, B.F.; De Vos, D.E. Patterned growth of metal-organic framework coatings by electrochemical synthesis. *Chem. Mater.* **2009**, *21*, 2580–2582. [CrossRef]
23. Zhang, B.; Luo, Y.; Kanyuck, K.; Saenz, N.; Reed, K.; Zavalij, P.; Mowery, J.; Bauchan, G. Facile and template-free solvothermal synthesis of mesoporous/macroporous metal–organic framework nanosheets. *RSC Adv.* **2018**, *8*, 33059–33064. [CrossRef] [PubMed]
24. Shekhah, O.; Chernikova, V.; Belmabkhout, Y.; Eddaoudi, M. Metal–organic framework membranes: From fabrication to gas separation. *Crystals* **2018**, *8*, 412. [CrossRef]
25. Biesinger, M.C.; Lau, L.W.; Gerson, A.R.; Smart, R.S.C. Resolving surface chemical states in XPS analysis of first row transition metals, oxides and hydroxides: Sc, Ti, V, Cu and Zn. *Appl. Surf. Sci.* **2010**, *257*, 887–898. [CrossRef]
26. Bradshaw, D.; Garai, A.; Huo, J. Metal–organic framework growth at functional interfaces: Thin films and composites for diverse applications. *Chem. Soc. Rev.* **2012**, *41*, 2344–2381. [CrossRef]
27. Yim, C.; Jeon, S. Direct synthesis of Cu-BDC frameworks on a quartz crystal microresonator and their application to studies of n-hexane adsorption. *RSC Adv.* **2015**, *5*, 67454–67458. [CrossRef]
28. Salama, R.S.; El-Hakam, S.; Samra, S.; El-Dafrawy, S.; Ahmed, A. Adsorption, equilibrium and kinetic studies on the removal of methyl orange dye from aqueous solution by using of copper metal organic framework (Cu-BDC). *Int. J. Mod. Chem* **2018**, *10*, 195–207.
29. Falcaro, P.; Okada, K.; Hara, T.; Ikigaki, K.; Tokudome, Y.; Thornton, A.W.; Hill, A.J.; Williams, T.; Doonan, C.; Takahashi, M. Centimetre-scale micropore alignment in oriented polycrystalline metal–organic framework films via heteroepitaxial growth. *Nat. Mater.* **2017**, *16*, 342–348. [CrossRef]
30. Shete, M.; Kumar, P.; Bachman, J.E.; Ma, X.; Smith, Z.P.; Xu, W.; Mkhoyan, K.A.; Long, J.R.; Tsapatsis, M. On the direct synthesis of Cu (BDC) MOF nanosheets and their performance in mixed matrix membranes. *J. Membr. Sci.* **2018**, *549*, 312–320. [CrossRef]
31. Sutapa, I.W.; Palapessya, B.V.; Souhoka, F.A.; Bandjar, A. Synthesis of Cu-1, 4-Benzene Dicarboxylate Metal-Organic Frameworks (Cu-BDC MOFs) from Plastic Waste and Its Application as Catalyst in Biodiesel Production. *Trends Sci.* **2024**, *21*, 7163. [CrossRef]
32. Abdelhamid, H.N. MOFTextile: Metal-organic frameworks nanosheets incorporated cotton textile for selective vapochromic sensing and capture of pyridine. *Appl. Organomet. Chem.* **2023**, *37*, e7078. [CrossRef]
33. Lubezky, A.; Chechelnitsky, L.; Folman, M. IR spectra of CH_4, CD_4, C_2H_4, C_2H_2, CH_3OH and CH_3OD adsorbed on C60 films. *J. Chem. Soc. Faraday Trans.* **1996**, *92*, 2269–2274. [CrossRef]
34. Azzolina-Jury, F.; Thibault-Starzyk, F. Mechanism of low pressure plasma-assisted CO_2 hydrogenation over Ni-USY by microsecond time-resolved FTIR spectroscopy. *Top. Catal.* **2017**, *60*, 1709–1721. [CrossRef]
35. Mojet, B.L.; Ebbesen, S.D.; Lefferts, L. Light at the interface: The potential of attenuated total reflection infrared spectroscopy for understanding heterogeneous catalysis in water. *Chem. Soc. Rev.* **2010**, *39*, 4643–4655. [CrossRef] [PubMed]
36. Chae, I.; Lee, D.; Kim, S.; Thundat, T. Electronic nose for recognition of volatile vapor mixtures using a nanopore-enhanced opto-calorimetric spectroscopy. *Anal. Chem.* **2015**, *87*, 7125–7132. [CrossRef]
37. Hong, T.; Culp, J.T.; Kim, K.-J.; Devkota, J.; Sun, C.; Ohodnicki, P.R. State-of-the-art of methane sensing materials: A review and perspectives. *TrAC Trends Anal. Chem.* **2020**, *125*, 115820. [CrossRef]
38. Xu, H.; Li, J.; Fu, Y.; Tian, Y.; Yang, Z. Sensitized mechanism of recovered S-SnO2 from tin sludge for CH4 detection by increasing oxygen vacancy density as an efficient strategy. *Sens. Actuators B Chem.* **2019**, *298*, 126838. [CrossRef]
39. Singh, M.; Raghuwanshi, S.K.; Prakash, O. Ultra-sensitive fiber optic gas sensor using graphene oxide coated long period gratings. *IEEE Photonics Technol. Lett.* **2019**, *31*, 1473–1476. [CrossRef]

40. Crawford, S.E.; Kim, K.-J.; Yu, Y.; Ohodnicki, P.R. Rapid, selective, ambient growth and optimization of copper benzene-1, 3, 5-tricarboxylate (Cu–BTC) metal–organic framework thin films on a conductive metal oxide. *Cryst. Growth Des.* **2018**, *18*, 2924–2931. [CrossRef]
41. Moslein, A.F.; Gutierrez, M.; Cohen, B.; Tan, J.-C. Near-field infrared nanospectroscopy reveals guest confinement in metal–organic framework single crystals. *Nano Lett.* **2020**, *20*, 7446–7454. [CrossRef]
42. Aprilia, L.; Nuryadi, R.; Saputro, A.G.; Wella, S.A.; Isa, I.M.; Bakar, S.A.; Neo, Y.; Mimura, H. Improved CH 4 Detection Utilizing Pt-decorated ZnO Nanorods-coated on a Dynamic Microcantilever Surface. *IEEE Sens. J.* **2024**, *24*, 29806–29813. [CrossRef]
43. Xu, J.; Setiono, A.; Peiner, E. Piezoresistive microcantilever with SAM-modified ZnO-nanorods@ silicon-nanopillars for room-temperature parts-per-billion NO2 detection. *ACS Appl. Nano Mater.* **2020**, *3*, 6609–6620. [CrossRef]
44. Liu, Y.; Tian, Y.; Lin, C.; Miao, J.; Yu, X. A monolithically integrated microcantilever biosensor based on partially depleted SOI CMOS technology. *Microsyst. Nanoeng.* **2023**, *9*, 60. [CrossRef] [PubMed]
45. Jeong, H.-J.; Kim, K.; Kim, H.W.; Park, Y. Classification between normal and cancerous human urothelial cells by using Micro-Dimensional Electrochemical Impedance Spectroscopy Combined with Machine Learning. *Sensors* **2022**, *22*, 7969. [CrossRef] [PubMed]

Disclaimer/Publisher's Note: The statements, opinions and data contained in all publications are solely those of the individual author(s) and contributor(s) and not of MDPI and/or the editor(s). MDPI and/or the editor(s) disclaim responsibility for any injury to people or property resulting from any ideas, methods, instructions or products referred to in the content.